*J. Synchrotron Rad.* (2000). **7**, 395–404

# Illumination for coherent soft X-ray applications: the new X1A beamline at the NSLS

**B. Winn,[a] H. Ade,[b] C. Buckley,[c] M. Feser,[a] M. Howells,[d] S. Hulbert,[e] C. Jacobsen,[a] K. Kaznacheyev,[a] J. Kirz,[a]* A. Osanna,[a] J. Maser,[a]† I. McNulty,[f] J. Miao,[a]‡ T. Oversluizen,[g] S. Spector,[a]§ B. Sullivan,[a]¶ Yu. Wang,[a]†† S. Wirick[a] and H. Zhang[b]‡‡**

*[a]Department of Physics and Astronomy, SUNY at Stony Brook, Stony Brook, NY 11794-3800, USA, [b]Department of Physics, North Carolina State University, Raleigh, NC 27599, USA, [c]Physics Department, King's College, London WC2R 2LS, UK, [d]Advanced Light Source, Lawrence Berkeley National Laboratory, Berkeley, CA 94720, USA, [e]National Synchrotron Light Source, Brookhaven National Laboratory, Upton, NY 11973, USA, [f]Advanced Photon Source, Argonne National Laboratory, Argonne, IL 60439, USA, and [g]Creative Instrumentation, 412 South Country Road, East Patchogue, NY 11772, USA. E-mail: janos.kirz@sunysb.edu*

(*Received 19 July 2000; accepted 19 September 2000*)

The X1A soft X-ray undulator beamline at the NSLS has been rebuilt to serve two microscopy stations operating simultaneously. Separate spherical-grating monochromators provide the resolving power required for XANES spectroscopy at the C, N and O absorption edges. The exit slits are fixed and define the coherent source for the experiments. The optical design and the operational performance are described.

**Keywords: beamlines; microscopy; coherence; soft X-rays; undulators.**

## 1. Introduction

Coherence in the visible range of the electromagnetic spectrum is routinely obtained using lasers. Lasers in the soft X-ray regime have been developed and used for microscopy (DaSilva *et al.*, 1992) and holography (Trebes *et al.*, 1987). Nevertheless, their time-averaged brightness, wavelength range and accessibility are currently still inferior to that available at synchrotron radiation sources.

Historically, coherence was imposed on photon beams by appropriate collimation (spatial coherence) and monochromatization (temporal coherence). In fact, holography was invented and first demonstrated this way (Gabor, 1949). Aoki and Kikuta (Aoki *et al.*, 1972) carried out the first holography experiments in the soft X-ray range using synchrotron radiation. Work at the NSLS with coherent beams began in 1982 (Rarback *et al.*, 1984). Kondratenko & Skrinsky (1977) pointed out that the coherent intensity obtained by collimation from an incoherent source is directly proportional to the source brightness, and that undulators are therefore particularly suitable sources for coherence-based experiments. The original X1A beamline [and its temporary predecessor (Rarback *et al.*, 1988)] was the first undulator beamline designed for coherence-based experiments (Howells *et al.*, 1982; Jacobsen & Rarback, 1985; Rarback *et al.*, 1990). Its experimental program has included scanning microscopy (Jacobsen *et al.*, 1991; Kirz *et al.*, 1995), scanning photoemission microscopy (Ade *et al.*, 1990) and diffraction from micrometer-sized non-crystalline samples (Sayre & Chapman, 1995), as well as holography (Jacobsen *et al.*, 1990; McNulty *et al.*, 1992; Lindaas *et al.*, 1996).

Here we report on a major upgrade of this undulator-based soft X-ray beamline. The goal of the upgrade was to create two independently tunable branches, each with higher flux and higher energy resolution than available previously. We were motivated principally by the needs of XANES microscopy (Ade *et al.*, 1992; Buckley & Zhang, 1998), a technique developed since the original beamline design, but now a dominant use of our microscopes. The outboard branch is home to the scanning transmission X-ray microscope (STXM) (Jacobsen *et al.*, 1991) with a user program in heavy demand. The inboard branch is time-

† Present address: Advanced Photon Source, Argonne National Laboratory, Argonne, IL 60439, USA.
‡ Present address: Stanford Synchrotron Radiation Laboratory, Stanford, CA 94025, USA.
§ Present address: MIT Lincoln Laboratory, Lexington, MA 02420-9108, USA.
¶ Present address: AIL Systems Inc., Deer Park, NY 11729, USA.
†† Present address: Xradia Inc., 4075A Sprig Drive, Concord, CA 94520, USA.
‡‡ Present address: 2283 Eglinton Avenue East, Toronto 2N4 M1K, Canada.

shared between the new cryo-STXM (Maser *et al.*, 1997, 2000; Wang *et al.*, 2000) and the new room-temperature STXM nearing completion (Feser *et al.*, 2000).

Our choices for the design are governed by the need to match the source characteristics to the experimental requirements. A typical scanning X-ray microscope uses a zone plate optic to demagnify a small source. The resulting spot profile is a convolution of the demagnified source size and the point spread function of the optic. For the optic, the phase space acceptance for diffraction-limited performance is the product of the full-angle acceptance, 2NA, and the diffraction-limited spot diameter (twice the Rayleigh resolution), 1.22λ/NA, *i.e.* 2.44λ, where NA is the zone plate numerical aperture. In Fig. 1 we show the convolved spot profile characterized in terms of a parameter $p$ equal to the source size multiplied by the full-angle accepted divided by the wavelength λ. We see that to obtain high spatial resolution we can accept a wavelength-normalized phase space area $p$ no larger than about 1 in each transverse direction (Buckley, 1988). Similar conclusions are obtained using the van Cittert-Zernike theorem for guidance in restricting an extended source to obtain a high degree of spatial coherence (Born & Wolf, 1999).

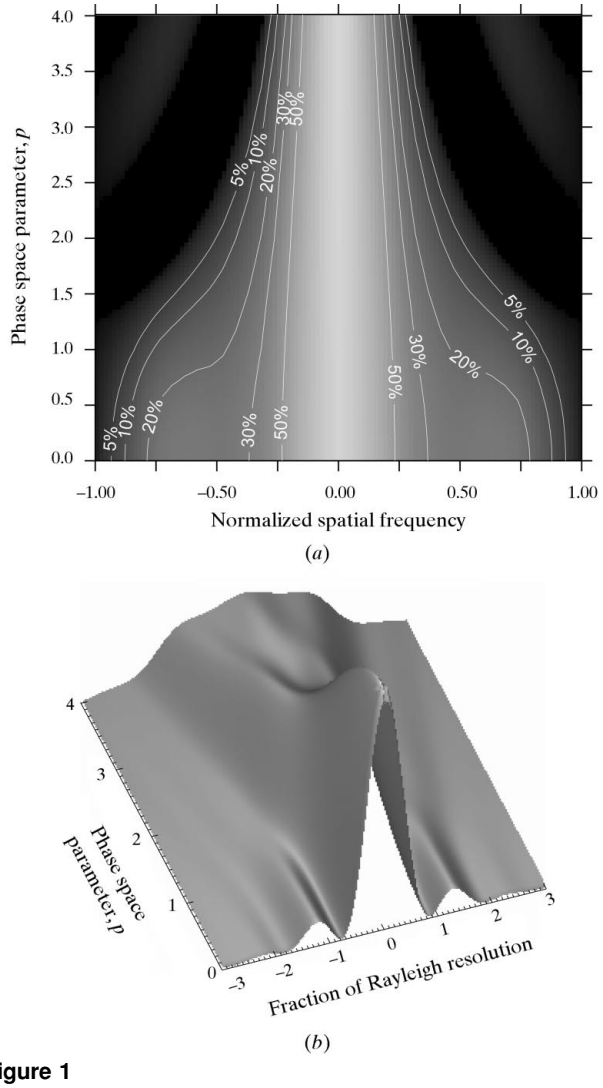


**Figure 1**
Calculation of the effect of partially coherent illumination of the zone plate on image quality and resolution for a zone plate with a central stop of half the zone plate diameter. (*a*) Contours of the modulation transfer function as a function of the coherence parameter, $p$ (equal to the source size multiplied by the full-angle accepted divided by the wavelength λ), and the normalized spatial frequency (spatial frequency divided by λ/4NA, where NA is the numerical aperture). (*b*) Surface rendering of the point spread function as a function of the coherence parameter, $p$, and the radial coordinate normalized to the Rayleigh resolution. Full spatial resolution is preserved for $p \leq 1$.

The phase space area of an undulator source is given by a convolution between the phase space area of the radiation emitted by one electron (Green, 1976; Krinsky, 1983; Kim, 1986) and the phase space area of the electron beam (its emittance $\varepsilon$). For the NSLS X-ray ring, $\varepsilon_x = 296$ nm rad, or about 75 times the 4 nm wavelength used in many of our experiments, and $\varepsilon_y = 2.5$ nm rad, which is less than a 4 nm wavelength. We are therefore able to use only about 1% of the horizontal output, but the full vertical output of the source for each experiment. This consideration dictated the basic layout of the beamline, where we take two small angular 'slices' from near the center of the horizontal fan for two different monochromators and end stations and image the full vertical extent of the source onto our exit slit.

The relatively large horizontal emittance of the NSLS X-ray ring also affects the undulator spectrum by including radiation from a range of single-electron emission angles observed on-axis. The resulting calculated spectrum from the X-1 undulator (Fig. 2) shows that all harmonics are broadened, and even harmonics are quite strong on-axis. This allows XANES experiments to scan an edge without

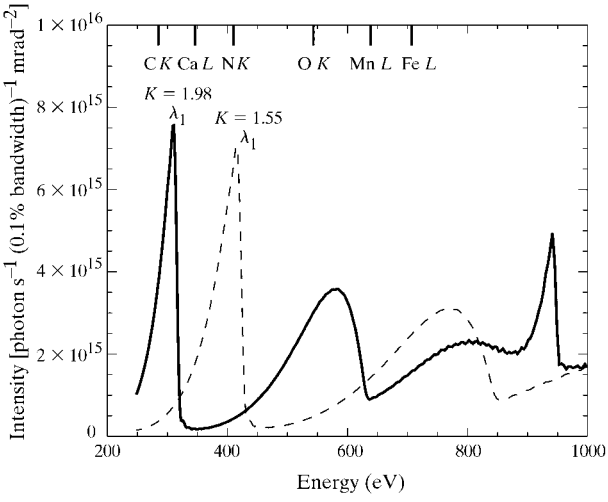


**Figure 2**
Calculated undulator output for two selected magnetic field parameters, $K$. For $K = 1.98$ the undulator fundamental covers the region near the C $K$-absorption edge while the second harmonic provides good intensity near the O $K$-edge. $K = 1.55$ is optimized for the region of the nitrogen $K$- and iron $L$-absorption edges. The presence of the second harmonic peaks on-axis is due to the finite electron beam divergence in the low-$\beta$ straight section where the undulator is located.

**Table 1**
Table of distances and deflection angles.

| | Outboard distance (m) | Branch angle (mrad) | Inboard distance (m) | Branch angle (mrad) |
|---|---|---|---|---|
| Mirror M0 | 12.95 | 80 | 12.95 | 80 |
| Mirrors M1 | 16.3 | 100 | 17.8 | 80 |
| Entrance slits ENS | 18.3 | | 20.05 | |
| Gratings G | 19.7 | 113.4 | 21.45 | 113.4 |
| Exit slits EXS | 23.6 | | 25.35 | |
| STXM | 24.8 | | 26.41 | |
| Cryo STXM | | | 27.25 | |

needing to tune the gap, and one endstation to work with the first harmonic around the C edge while the other endstation works with the second harmonic near the O edge.

For scanning microscopy experiments the smallest probe size can be no better than the diffraction-broadened demagnified size of the monochromator exit slit for reasons shown in Fig. 1. This consideration dictates the size of the exit slit for best spatial resolution.† However, different experiments have different requirements for energy resolution (in particular, quantitative microscopy using XANES resonances requires good energy resolution). We have therefore chosen a monochromator layout where the energy resolution is determined primarily by the adjustment of the entrance-slit size rather than the exit-slit size, as long as the exit slit is smaller than the entrance slit. In this arrangement, where one determines the spatial resolution mostly by exit-slit size and spectral resolution by entrance-slit size, one can more efficiently trade flux for energy resolution when desired.

The new beamline has the following special features:

(i) The beam is split into three branches using scraping mirrors.

(ii) The source is imaged horizontally onto the monochromator entrance slits and vertically onto the exit slits using toroidal mirrors.

(iii) Spherical-grating monochromators with fixed exit arms are used. Good spectral resolution is achieved because the coherent part of the beam has a small footprint on the grating, and therefore aberrations remain small.

(iv) The stigmatic focus at the exit slit becomes the source for coherence-based experiments. For a given experimental arrangement the size of the slits at the focus sets the required spatial coherence. The resolving power of the monochromator is adjusted using the entrance slit alone, providing a favorable resolution/flux trade-off (Ade, 1998).

The optical layouts of the two branches are almost identical. A schematic diagram is shown in Fig. 3. The layout is shown in Fig. 4. Distances, deflection angles and design parameters of the optical elements are listed in Table 1. The beamlines are designed to deliver the coherent portion of the beam (a single mode in laser terminology) to the experiments, although a larger intensity can also be obtained by opening the slits. To define the degree of spatial coherence requires two apertures: the first is the exit slit and the second is the aperture at the experiment, in our case mostly the zone plate. We select the degree of coherence desired for the experiments and overfill the apertures to reduce the sensitivity to vibrations and drifts. We are not dealing with a very large power or even large power densities on the optical elements past the first one. This allows us to use relatively simple and inexpensive components, which are described below.

† For the effects of incoherent or partially coherent illumination on resolution in X-ray microscopes, see Jacobsen *et al.* (1992), Jochum & Meyer-Ilse (1995) and Vogt *et al.* (2000).

## 2. Beamline components

The undulator and the first part of the beamline are unchanged from the original (Rarback *et al.*, 1990). The 35-period undulator, with a period of 8 cm and a minimum gap of 32 mm, is located in a low-$\beta$ section of the X-ray ring. The emittance of the ring has been reduced over the years, and the parameters of the current operation are given in Table 2 (Safranek, 1998).

The beam is first split using the water-cooled plane scraping mirror (DiGennaro *et al.*, 1988), which intercepts about 35% of the central cone. This Ni-coated mirror deflects the beam by 80 mrad horizontally in the outboard direction. It absorbs essentially all the radiation above 2 keV and reduces the power on the optical elements that follow to 40 W or less. [The undeflected beam feeds the X1B spectroscopy beamline (Randall *et al.*, 1992).] The reflected beam is collimated using a water-cooled Cu mask. Beamline components beyond this mask are all replaced as follows:

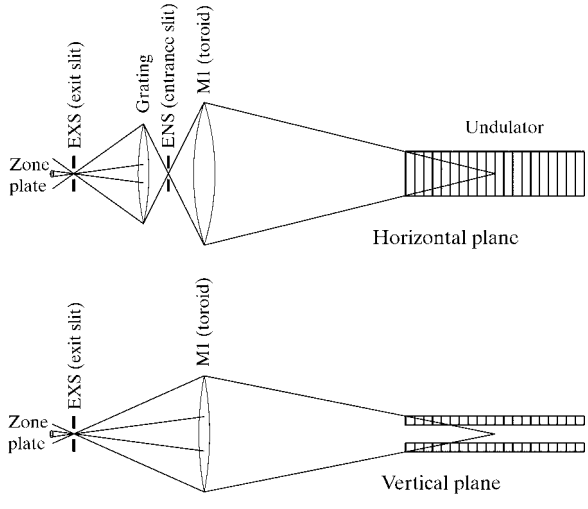


**Figure 3**
Schematic diagram of the beamline optics for the outboard branch. Note that the zone plate is overfilled in both the horizontal and vertical plane. Only a small area of the grating contributes to the illumination of the zone plate. As a result, the effect of aberrations on energy resolution is small even with a fixed exit slit.

**Table 2**
Source parameters.

All values shown are for FWHM.

| | Electron beam parameters | | | |
|---|---|---|---|---|
| Undulator source parameters | 1990 values | Current values | X-ray at 4.3 nm from single electron | X-ray at 4.3 nm† full beam current |
| Horizontal size (μm) | 917 | 637 | 20.4 | 637 |
| Horizontal divergence (μrad) | 588 | 456 | 92 | 465 |
| Vertical size (μm) | 42 | 14 | 20 | 25 |
| Vertical divergence (μrad) | 141 | 40 | 92 | 100 |

† Electron beam and X-ray values added in quadrature.

(i) The beam is split again (this time 50%–50%) using a second scraping mirror. This mirror is the toroid that focuses the beam horizontally onto the entrance slit and vertically onto the exit slit for the outboard branch. It deflects horizontally outboard by 100 mrad. The major and minor radii are 70.6 m and 0.509 m, respectively. The horizontal magnification produced by this mirror is 0.123, while the vertical magnification is 0.48.

(ii) The undeflected part of the beam intercepts a second similar toroid, which plays the same focusing role for the inboard branch. It deflects outboard by 80 mrad. The major and minor radii are 100.6 m and 0.426 m, respectively. This mirror provides a horizontal magnification of 0.126 and a vertical magnification of 0.42. Both toroids are made from single-crystal silicon blanks and are gold-coated over the footprint of the beam. The RMS roughness is less than 0.5 nm, and the figure accuracy is better than 15 μrad over the footprint of the beam. The mirrors were manufactured by Continental Optical Corporation (Hauppauge, NY 11788, USA). They are mounted on modified supports (McPherson Inc., Chelmsford, MA 01824, USA) which provide water-cooling from the back and a three-point kinematic adjustment of the orientation of the mirror normal. In addition, the custom modification allows us to make small yaw adjustments by axially twisting the bellows which couple the kinematic mount to the mirror vacuum chamber. Once the beamline is aligned, these adjustments remain fixed.

(iii) The toroids focus the beam horizontally onto custom-designed water-cooled entrance slits (Fig. 5). Each of these devices carries a selection of fixed slits with widths of 10, 25, 40, 70, 120, 200 μm and fully open. The slits are made in a single sheet of 0.37 mm-thick nickel-coated beryllium–copper (Photo Sciences Inc., Torrance, CA 90505, USA). This thin sheet is sandwiched between the water-cooled backing and a cover plate; both are made of copper. The assembly with the water-cooling pipes forms a rigid system that is driven by a stepping motor through a bellows seal relative to the beam. There are no water-to-vacuum seals. A fixed copper mask with a 3 mm hole assures that no stray light can sneak past without passing through the slit selected. Beam on the slits can be observed through mini-viewports. The slit assemblies can be scanned horizontally under computer control to center the chosen slit on the beam, or to measure the beam shape at these locations.

(iv) Samson-type (Samson, 1967) aluminium photodiodes are mounted just downstream of the entrance slits to monitor the beam intensity at these points. The aluminium surface, when inserted into the beam, acts as the photoemitter. It also acts as a manual shutter. It can handle the full beam power at this point without cooling, except at small undulator gaps.

(v) Grating masks are mounted just upstream of the grating chambers. Four independently adjustable linear feedthroughs carry blades that can restrict the height and

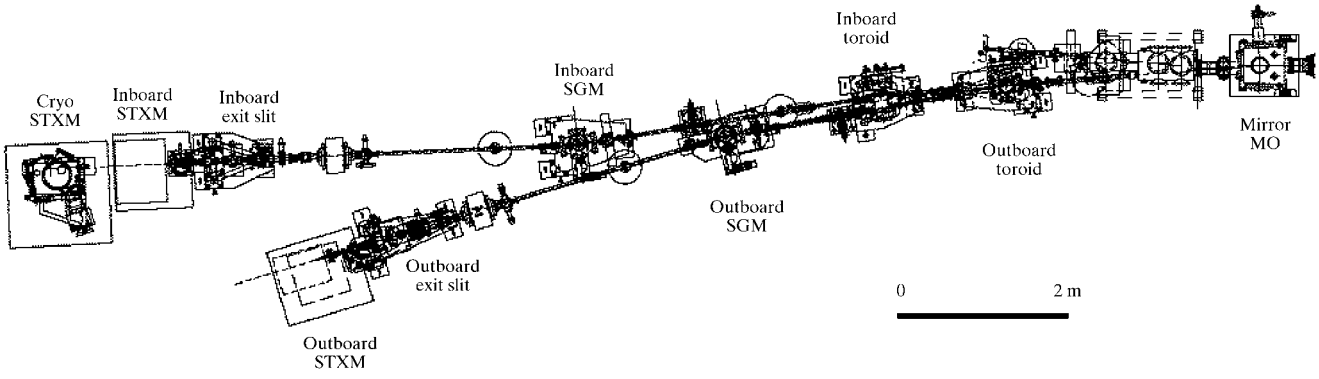


**Figure 4**
Layout of the beamline showing the components outside the shield wall which is located just at the right-hand edge of the diagram.

width of the beam on the gratings. The visible component of the beam on these blades can be observed through standard viewports.

(vi) The horizontally dispersing spherical gratings are mounted on a precision spindle with a sine arm mechanism. The sine arms are moved using stepper motors with encoders. The laminar gratings were fabricated by Tayside Optical Technology (now Spectrogon UK Ltd, Glenrothes, Fife KY6 2TF, UK) in single-crystal silicon blanks. The blank size is 125 mm × 65 mm × 35 mm. The radii are 45.49 m (outboard) and 46.41 m (inboard). The groove density of both gratings is 892 lines $mm^{-1}$, the RMS roughness is less than 0.5 nm, and the figure error is less than 3 μrad. The grating used on the outboard branch has a groove depth of 12.5 nm and a land:groove ratio of 1:1.5, while the corresponding parameters for the inboard branch are 9.0 nm and 1:1.4. The ruled area has a gold coating. The groove depths were designed to provide good efficiency in the energy range of interest. Calculated grating efficiencies are shown in Fig. 6. At the exit port of the grating chambers stainless steel blades are mounted to stop the zeroth-order beam from the grating in normal operation. One can observe the visible portion of the beam on the gratings and on the stops through large viewports facing the gratings. The mechanism has been designed with careful attention to accuracy and reproducibility, and it performs satisfactorily without feedback controls.

(vii) Just upstream of the exit slits there are two instrumentation crosses. The first of these has a linear feedthrough that carries a phosphor pad and a small aluminium plate that is electrically isolated from the rest of the beamline. The phosphor pad is used as a beam finder during alignment. The aluminium plate has a 2 mm hole in the center to allow the beam of the selected wavelength to pass through, but it intercepts neighboring parts of the spectrum. It is connected through a BNC feedthrough to a shielded 9 V battery. We can monitor the beam intensity at this point by recording the photoemission current to the battery.

(viii) The second instrumentation cross carries a set of fixed slits, identical to the entrance slits, but these are not water-cooled. They are horizontal slits to measure and define the vertical extent of the beam at the monochromator exit slit. We refer to these as the vertical exit slits. They are mounted on a linear feedthrough driven by a stepper motor.

(ix) The monochromator exit slits follow the vertical slits. These are continuously adjustable through a flexure mechanism, and define the horizontal extent of the beam at this point.

(x) The intensity of the beam past the exit slits is monitored using aluminium vacuum photodiodes, which also act as fast computer-controlled shutters (Chapman *et al.*, 1999).

From this point on, the two branches differ. On the outboard branch we have the option of inserting an order-sorting device, based on a pair of parallel grazing-incidence plane mirrors (Hazel *et al.*, 1998). Since much of the motivation for the new beamline is to perform chemical state mapping (often quantitative) using XANES peaks, it is important that absorption measurements are not distorted by background introduced by higher-order spectral contamination (Buckley, 2000). The outboard branch makes extensive use of absorption resonances at the C *K*-edge where higher-order contamination can be a problem. To optimize both throughput and higher-order rejection, the grazing angle on the mirror system was chosen to provide a >99% second-order rejection at 285 eV. The amount of second order reaching the specimen is further reduced by the use of zone plates with a central stop followed by an order-sorting aperture of slightly smaller diameter that accepts the first-order focused beam but rejects unwanted orders. The combined suppression is such

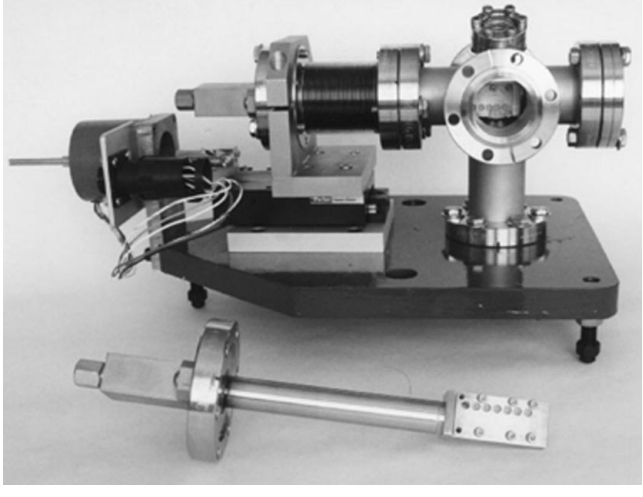

**Figure 5**
Photograph of the entrance slit assembly viewed from the upstream side. A series of fixed slits can be positioned in the beam by using the stepper motor to translate the water-cooled insert, also shown separately in the foreground.

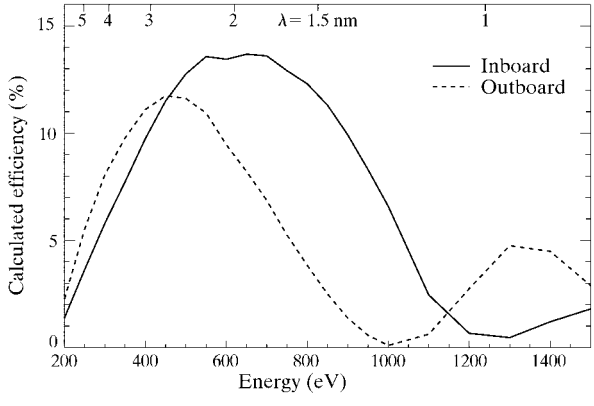


**Figure 6**
Calculated efficiency of our diffraction gratings. The outboard grating is optimized for operation near the C, N and O *K*-absorption edges. The inboard grating has higher efficiency in the 700–900 eV range.

**Table 3**
Predicted and measured beam sizes.

The measured values depend on actual storage ring operating conditions and vary by up to 30%. The smallest measured values are shown. All values shown are for FWHM (μm).

| | Beam size | | |
|---|---|---|---|
| | Predicted at focus | Predicted at measurement | Measured |
| Outboard entrance slit | 78 | 78 | 100 |
| Inboard entrance slit | 80 | 80 | 117 |
| Outboard exit slit | 12 | 26† | 24 |
| Inboard exit slit | 11 | 25† | 21 |

† Measured 0.1 m upstream of focus.

that errors introduced to absorption measurements are always below the uncertainty set by photon statistics for all realistic pixel dwell times. Following the order-sorting mirrors, the beam passes through the central opening in an Si quadrant photodiode (International Radiation Detectors, Torrance, CA 90505-5229, USA) that senses the beam position in front of the experimental station.

On the inboard branch we have a similar pair of parallel mirrors for order sorting, and the additional option of inserting a device to split the beam for Nomarski interference microscopy (Polack *et al.*, 2000; Carlucci-Dayton, 2000).

Once the toroids and spherical gratings were delivered by the manufacturer, their radii of curvature were carefully measured. The final layout of the beamline was then adjusted to fit the measured values.

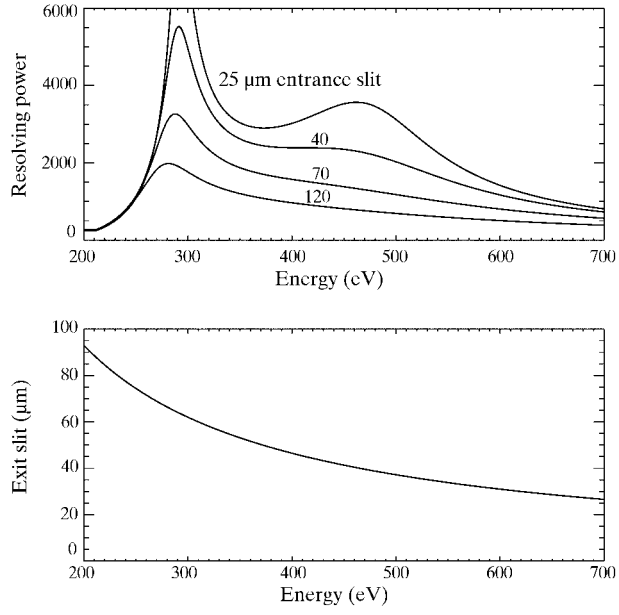


**Figure 7**
Calculated resolving power and the required exit-slit width when the beam illuminates an 80 μm-diameter zone plate at 1.2 m from the exit slit with coherence parameter $p = 1$.

## 3. Optical design

### 3.1. *Spherical-grating monochromator*

The spherical-grating monochromator design for the two branches is identical. The entrance arm is 1.4 m, the exit arm is 3.9 m, and the instrument operates in positive first order. For a traditional spherical grating on the Rowland circle the distance to the exit slit must be adjusted as the grating rotates to keep the slit at the proper focal distance.

However, for the very narrow beams we are dealing with, defocus aberration is small and good resolution can be obtained with a fixed exit arm length. What matters in the calculation is not the area on the grating that is illuminated by the beam, but rather the area of the grating that contributes to the illumination of the experiment (the zone plate, for example). Aside from the simplicity and savings in cost, this arrangement makes it easy to mount the experiment in a fixed position, relatively close to the exit slit. To optimize performance, the exit arm length is chosen so that the monochromator is in focus near the O and C absorption edges. Resolution suffers little at energies in between, but deteriorates rapidly outside this range, as illustrated in Fig. 7.

### 3.2. *Imposing the spatial coherence requirement*

The X-1 undulator has a source size and divergence dominated by that of the electron beam. The electron beam is characterized by an emittance $\varepsilon = \sigma\sigma'$, where $\sigma$ and $\sigma'$ correspond to a Gaussian size and angle, respectively. The phase space area of the source is then $2\pi\sigma\sigma'$, but we can only accept a full-width size times angle product of $p\lambda$ with $p < 0.5$ for full spatial coherence or $p \simeq 1$ for almost diffraction-limited imaging (Jacobsen *et al.*, 1992). The coherence criterion is clearly wavelength dependent, and easier to satisfy at longer wavelengths. Near the C *K*-absorption edge the beam from the undulator is fully coherent in the vertical plane. We re-focus this beam to the exit slit, and possibly restrict it there further using our vertical slit, to form the source for experiments. Since the toroids and gratings deflect or disperse in the horizontal plane, vertical focusing is less sensitive to slope errors, and the coherence of the beam is thereby better preserved. The beam emerging from the exit slit is used to provide coherent illumination for the zone plate that is used to form the demagnified beam spot for the scanning microscope.

The zone plate is placed far enough from the exit slit to be overfilled. Overfilling leads to loss of coherent flux, but improves stability and uniformity of illumination. We can also place a slit in the vertical focus. This slit can be used to cut off the tails of the illumination, or to increase the overfilling factor and reduce the coherence parameter $p$. At shorter wavelengths a smaller slit can be used to provide the required coherence.

In the horizontal plane we accept 15% of the undulator fan in each branch. The horizontal image size on the entrance slit is given by the source size multiplied by the M1 mirror magnification, which in our case is about 100 μm

(Table 3). For experiments requiring only moderate temporal coherence (resolving power $\simeq 500$) we accept the full 15%, and reject only the tails of the distribution. If higher resolving power is needed, the entrance-slit size is reduced and the slit is overfilled. The spherical grating images the entrance slit roughly 1:1 onto the exit slit for a given energy. The width (horizontal plane) of the exit slit is adjusted to match the vertical image size (or the vertical slit size if it is smaller) to provide the optimum source size, both horizontally and vertically, for illumination of the zone plate. This choice generally results in a slit width small enough for good energy resolution; therefore we tend to run with the entrance-slit opening equal to or larger than the exit-slit opening. The divergence of the beam emerging from the exit slit is much larger in the horizontal plane than in the vertical plane, and the zone plate is comfortably overfilled.

For a given experimental geometry, if the best temporal and best spatial coherence are required then the entrance and exit slits must both be small, and we lose flux as the square of the slit size reduction factor relative to the slit size which accepts 100% of the source flux. This cannot be avoided. However, our design strategy allows us to gain back part of that which was lost if the temporal coherence requirement is relaxed by allowing the entrance-slit size to be increased. This is useful when both conventional and XANES microscopies (requiring low and high temporal resolution, respectively) must be performed on the same beamline.

The beam intensity on the zone plate is calculated in one of two ways. We can multiply the undulator brightness by the zone plate acceptance, or we can go down the beamline and impose the cuts in phase space represented by the various slits. (In either case the reflectivities of the mirrors and the efficiencies of the gratings must be included in the calculation.) We have chosen the latter of these approaches, and the result is shown in Fig. 8.

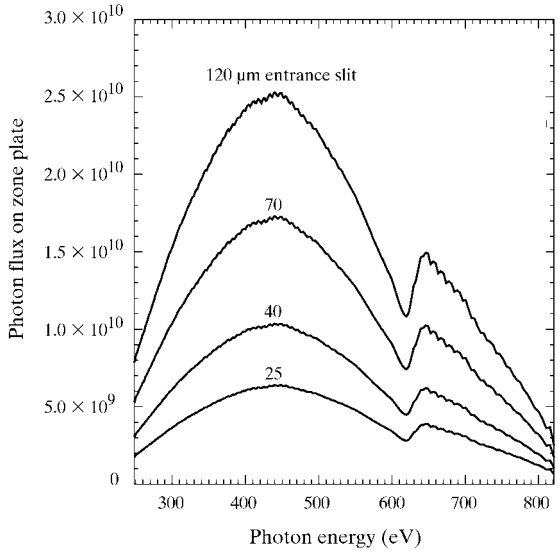


**Figure 8**
Calculated intensity incident on an 80 μm-diameter zone plate at 1.2 m from the exit slit for a 250 mA circulating electron beam and for the entrance-slit sizes indicated. The exit slit is set for coherence parameter $p = 1$. Note that the measured intensity in the zone plate focus is reduced by additional factors including the zone plate focusing efficiency (typically 10%), absorption in silicon nitride windows used for vacuum isolation, zone plate mounting and detector isolation, absorption losses in any atmospheric-pressure gas through which the beam must pass, and the use of order-sorting mirrors at the lower energies.

## 4. Systems considerations

### 4.1. *Dealing with power in the beam*

The first mirror (DiGennaro *et al.*, 1988) is made from a glidcop (alumina dispersion-strengthened copper) blank with internal water-cooling channels. It was designed to handle the full power of the undulator beam. Careful measurements (DiGennaro & Swain, 1990) have not revealed measurable distortions of its surface during actual use.

The next optical elements in the beamline absorb much less power. These are the toroids, which are made of single-crystal silicon. The material was chosen for its good thermal conductivity and low thermal expansion coefficient to minimize thermal distortion. The blanks are oversized (125 mm × 65 mm × 35 mm) to increase the rigidity and cooling surface area. The mirrors are cooled from the back. Gallium–indium eutectic is used to improve thermal conductivity to the water-cooled copper mounting plate. A thermocouple is attached to the side of each mirror. The measured temperature increase under operating conditions is less than 2 K. We have not observed any power-related beam motion or change in the focusing properties.

The water-cooled entrance slits have been described above. The power incident is 30 W or less and the power density is 150 W mm$^{-2}$ or less. With this power loading we have not observed any distortion or deterioration of the slits.

Components past the entrance slits are not water-cooled. The photodiodes and grating masks may become quite hot when called upon to intercept the beam with the entrance slits in the open position. However, small distortions of these components due to thermal expansion do not affect the performance of the beamline.

The gratings are made on silicon blanks, similar in size to the toroids. The large surface allows for efficient radiative cooling. When high resolving power is needed, the entrance slit is small and the incident power is negligible. When the entrance slit allows more of the beam to reach the grating, the resolution is limited by slit size rather than by thermal distortion. Under typical operating conditions the thermocouples attached to the side of the gratings show only a degree or two of temperature rise.

Most of the remaining power is absorbed on the zeroth-order stops.

### 4.2. *Vacuum system and safety interlock*

The X1A beamline vacuum is connected to the electron storage ring without windows. To satisfy NSLS vacuum requirements the beamline must operate at a pressure below $2 \times 10^{-9}$ torr. Furthermore, we wish to minimize the build-up of carbonaceous deposits on the optical surfaces, since a major part of the experimental program involves spectroscopy near the carbon *K*-absorption edge. This sets additional requirements on system cleanliness. To satisfy these requirements, each major component (mirror or grating) is housed in its own chamber with a $200\ \mathrm{l\ s^{-1}}$ or $400\ \mathrm{l\ s^{-1}}$ ion pump and titanium sublimator.

Additional ion pumps are installed in front of and behind the exit slits. Associated with each of these pumps are gate valves to allow parts of the beamline to be isolated, as well as ionization gauges, vent valves and Convectron gauges. Nevertheless, carbon contamination on the optical elements is a problem for C-edge spectroscopy, so we periodically clean the surfaces using UV light. (With the chamber vented to air, a UV lamp is held a few millimeters from the surface for several hours.)

The gate valves are pneumatically operated, and interlocked to ionization gauges located further downstream to avoid vacuum accidents. The interlock system uses an Allen Bradley SLC 500 programmable logic controller with eight input and output modules. These modules read the relay output of the gauges, open and close the pneumatic valves according to the vacuum conditions and provide power to the indicator lights on the interlock front panel and panels at the experimental stations.

An unusual aspect of the beamline is that a 100 nm-thick 200 μm × 200 μm silicon nitride membrane terminates the UHV system. Beyond that, experiments operate at atmospheric pressure. We now have almost 20 years of experience with these thin membranes, and they have proven to be reliable under our standard operating conditions. Nevertheless, we have an additional level of vacuum protection between this window and the upstream part of the beamline, in that the exit slits provide excellent differential pumping, being essentially gas-tight aside from their small openings.

### 4.3. *Alignment and stability*

To facilitate alignment and ensure stability, each major beamline element is mounted on kinematic supports from a welded stand bolted to the floor. The exception to this rule is the experimental apparatus at the end of each branch, which stands on vibration isolation tables with 30 μm repeatability in the vertical plane (Newport Corporation, Irvine, CA 92714, USA). To minimize sensitivity to floor vibrations, drifts and shifts of the vibration isolation table, we overfill all apertures. In the vertical, where, for longer wavelengths, the entire beam from the undulator is sufficiently coherent, this involves some loss in intensity at the experiment. In the horizontal plane we accept more than the coherent beam all the way to the last aperture that defines the experiment. (In our microscopes this is the zone plate.) The temperature on the experimental floor is generally stable enough so that we have not seen the need to add further thermal regulation of the apparatus.

The position of the slits and the sine arms of the gratings are controlled using stepper motors interfaced through an E500 CAMAC module to a VAX station. This control system will be replaced by a PC running the LINUX operating system in the near future.

**Table 4**
Predicted and measured intensity incident on the zone plate on the outboard branch at a wavelength of 3.22 nm (385 eV), a circulating beam current of 250 mA and with the order-sorting mirrors removed.

Measurements were corrected for absorption in two silicon nitride windows and in 8 mm of atmospheric helium. At this energy, 1 nA of photodiode current corresponds to $6.0 \times 10^7$ photons $\mathrm{s^{-1}}$. The measured values depend on actual storage ring operating conditions and vary by up to 30%. Typical measured values are shown.

| | | Intensity ($\times 10^9$ photons $\mathrm{s^{-1}}$) | |
|---|---|---|---|
| Entrance slit (μm) | Exit slit (μm) | Measured | Calculated |
| 25 | 25 | 2 | 2.8 |
| 40 | 25 | 3.2 | 4.5 |
| 40 | 40 | 6.9 | 7.6 |
| 70 | 70 | 22 | 23 |
| 200 | 200 | 120 | 116 |

## 5. Performance

We characterized the beamline using silicon photodiodes with a 100 nm aluminium coating (International Radiation Detectors) to reduce visible-light sensitivity. These photodiodes are absolutely calibrated by the manufacturer. We also used the shutter photodiodes, which we calibrated against the silicon devices. Photodiodes located just downstream of the exit slits were used to measure the horizontal beam size at the entrance slits and the vertical beam size at the exit slits, by scanning a 10 μm-wide slit across the beam. Results of these measurements are indicated in Table 3.

We measured the intensity incident on the zone plate by placing an aperture of the appropriate diameter at the zone plate location followed by a silicon photodiode (International Radiation Detectors). In Table 4 we present the comparison between these measurements and calculations much like the ones shown in Fig. 8. The agreement is better than we would expect based on the uncertainties associated with the measurements.

To study the resolving power of the monochromators, we measured the spectrum near the $1s \rightarrow \pi^*$ resonance in molecular nitrogen. We used a similar silicon photodiode in the vacuum chamber of the cryomicroscope filled with air to a pressure of 10 mtorr to obtain spectra in transmission, one of which is shown in Fig. 9. By fitting these with Voigt functions, we determined the resolving power as a function

of slit size. We found a resolving power of 3600 for 25 μm entrance and exit slits and 2400 for 40 μm slits, in good agreement with the calculations shown in Fig. 7.

## 6. Operational experience

Our operational experience shows that the design goals have been met in that our two branches, as well as a third branch (X1B), operate simultaneously most of the time. Simultaneous operation with independent tuning of the energies in each branch is successful because of the nature of the undulator spectrum, illustrated in Fig. 2. For example, at an undulator gap of 39 mm there is good intensity available over a broad range of energies around the C and O *K*-absorption edges, as well as the *L*-edges of some of the transition elements, *i.e.* Fe, Co and Ni. The measured intensities and the resolving power of the monochromators are in good agreement with the design, giving higher-resolution spectra and faster image recording than before. In normal operations with local feedback tied to our beam-position monitors, the beam has proven stable and reliable, with no evidence of drifts or vibrations on any time scale.

For energies below 350 eV the monochromator passes enough intensity in the higher orders (two or three times the energy) that we find the order-sorting mirrors (Hazel *et al.*, 1998; Buckley, 2000) very useful both for spectroscopy and for imaging. (This is even more the case when the NSLS operates at 2.8 GeV, in addition to the traditional 2.54 GeV mode.)

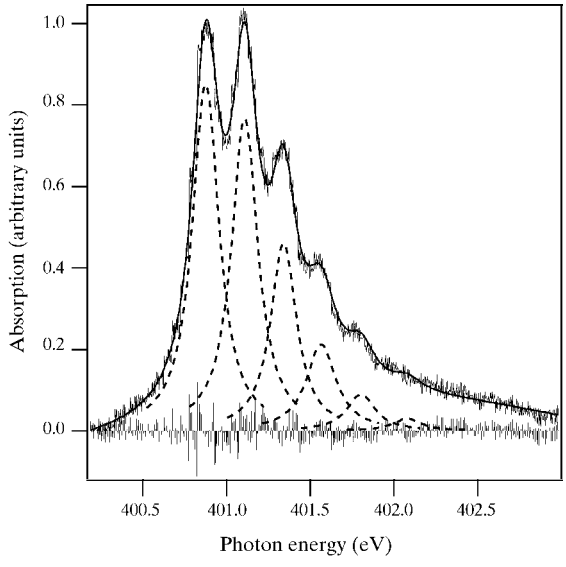


**Figure 9**
Fine structure in the spectrum of the nitrogen molecule near 401 eV, measured on the inboard branch using 25 μm slits. The experimental curve is shown, along with the fit to a set of Voigt functions and the residuals. The energy resolution given by the fit is 0.11 eV.

We acknowledge the help and advice of H. Chapman and J. Dickerson from Stony Brook, P. Takacs, Q.-Y. Dong, G. van der Laske, A. Lenhard and the NSLS vacuum group from Brookhaven, A. P. Smith from North Carolina State University, W. McKinney and V. Martynov from Berkeley Laboratory. We are grateful to the US Department of Energy, as well as our home institutions, and especially E. Gluskin, W. Yun, E. Johnson, P. Siddons and J. Hastings for generous support that made this project possible. The silicon photodiodes were provided by R. Korde, International Radiation Detectors. This work was performed at the NSLS, which is supported by the Department of Energy.

## References

Ade, H. (1998). Unpublished.
Ade, H., Kirz, J., Hulbert, S., Johnson, E., Anderson, E. & Kern, D. (1990). *Appl. Phys. Lett.* **56**, 1841–1843.
Ade, H., Zhang, X., Cameron, S., Costello, C., Kirz, J. & Williams, S. (1992). *Science*, **258**, 972–975.
Aoki, S., Ichihara, Y. & Kikuta, S. (1972). *Jpn. J. Appl. Phys.* **11**, 1857.
Born, M. & Wolf, E. (1999). *Principles of Optics.* Cambridge University Press.
Buckley, C. J. (1988). *X-ray Microscopy II*, edited by D. Sayre, M. Howells, J. Kirz & H. Rarback, pp. 146–150. Berlin: Springer.
Buckley, C. J. (2000). *X-ray Microscopy 1999*, edited by W. Meyer-Ilse, A. Warwick & D. T. Attwood, pp. 33–40. Melville: American Institute of Physics.
Buckley, C. J. & Zhang, X. (1998). *Proc. SPIE*, **3449**, 208–219.
Carlucci-Dayton, M. (2000). MSI thesis, SUNY, Stony Brook, New York, USA.
Chapman, H. N., Vogt, F. S., Jacobsen, C., Kirz, J., Miao, J., Winn, B., Wang, Y. & Oversluizen, T. (1999). *J. Synchrotron Rad.* **6**, 50.
DaSilva, L. B., Trebes, J. E., Balhorn, R., Mrowka, S., Anderson, E., Attwood, D. T., Barbee, T. W. Jr., Brase, J., Corzett, M., Gray, J., Koch, J. A., Lee, C., Kern, D., London, R. A., MacGowan, B. J., Matthews, D. L. & Stone, G. (1992). *Science*, **258**, 269–271.
DiGennaro, R., Gee, B., Guigli, J., Hogrefe, H., Howells, M. & Rarback, H. (1988). *Nucl. Instrum. Methods*, A**266**, 498–506.
DiGennaro, R. & Swain, T. (1990). *Nucl. Instrum. Methods*, A**291**, 313–318.
Feser, M., Beetz, T., Carlucci-Dayton, M. & Jacobsen, C. (2000). *X-ray Microscopy 1999*, edited by W. Meyer-Ilse, A. Warwick & D. T. Attwood, pp. 367–372. Melville: American Institute of Physics.
Gabor, D. (1949). *Proc. R. Soc. London Ser. A*, **197**, 454–487.
Green, G. K. (1976). Report BNL-50522. Brookhaven National Laboratory, Upton, NY 11973, USA.
Hazel, R., Buckley, C., Hao, X., Jacobsen, C., Kirz, J., Oversluizen, T., Winn, B. & Wirick, S. (1998). Unpublished.
Howells, M. R., Kirz, J. & Krinsky, R. (1982). Report 32519. Brookhaven National Laboratory, Upton, NY 11973, USA.
Jacobsen, C., Howells, M., Kirz, J. & Rothman, S. (1990). *J. Opt. Soc. Am.* A**7**, 1847–1861.
Jacobsen, C., Kirz, J. & Williams, S. (1992). *Ultramicroscopy*, **47**, 55–79.
Jacobsen, C. & Rarback, H. (1985). *Proc. SPIE*, **582**, 201–211.
Jacobsen, C., Williams, S., Anderson, E., Browne, M. T., Buckley, C. J., Kern, D., Kirz, J., Rivers, M. & Zhang, X. (1991). *Opt. Commun.* **86**, 351–364.
Jochum, L. & Meyer-Ilse, W. (1995). *Appl. Opt.* **34**(22), 4944–4950.
Kim, K.-J. (1986). *X-ray Data Booklet*, edited by D. Vaughhan, §4.1. Center for X-ray Optics, Berkeley, CA, USA.

Kirz, J., Jacobsen, C. & Howells, M. (1995). *Q. Rev. Biophys.* **28**, 33–130.
Kondratenko, A. M. & Skrinsky, A. N. (1977). *Opt. Spectrosc.* **42**, 189–192.
Krinsky, S. (1983). *IEEE Trans. Nucl. Sci.* NS-**30**, 3078–3082.
Lindaas, S., Howells, M., Jacobsen, C. & Kalinovsky, A. (1996). *J. Opt. Soc. Am.* A**13**, 1788–1800.
McNulty, I., Kirz, J., Jacobsen C., Anderson, E. H., Howells, M. R. & Kern, D. P. (1992). *Science*, **256**, 1009–1012.
Maser, J., Jacobsen, C., Osanna, A., Wang, S., Kalinovsky, A., Kirz, J., Spector, S. & Warnking, J. (1997). *X-ray Microscopy and Spectromicroscopy*, edited by J. Thieme, G. Schmahl, E. Umbach & D. Rudolph, pp. I-35–44. Berlin: Springer-Verlag.
Maser, J., Osanna, A., Wang, Y., Jacobsen, C., Kirz, J., Spector, S., Winn, B. & Tennant, D. (2000). *J. Microsc.* **197**, 68–79.
Polack, F., Joyeux, D., Feser, M., Phalippou, D., Carlucci-Dayton, M., Kaznacheyev, K. & Jacobsen, C. (2000). *X-ray Microscopy 1999*, edited by W. Meyer-Ilse, A. Warwick & D. T. Attwood, pp. 573–580. Melville: American Institute of Physics.
Randall, K. J., Feldhaus, J., Erlebach, W., Bradhsaw, A. M., Eberhardt, W., Xu, Z., Ma, Y. & Johnson, P. D. (1992). *Rev. Sci. Instrum.* **63**, 1367–1370.
Rarback, H., Buckley, C., Ade, H., Camillo, F., DiGennaro, R., Hellman, S., Howells, M., Iskander, N., Jacobsen, C., Kirz, J., Krinsky, S., Lindaas, S., McNulty, I., Oversluizen, M., Rothman, S., Sayre, D., Sharnoff, M. & Shu, D. (1990). *J. X-ray Sci. Technol.* **2**, 274–296.
Rarback, H., Jacobsen, C., Kirz, J. & McNulty, I. (1988). *Nucl. Instrum. Methods*, A**266**, 96–105.
Rarback, H., Kenney, J. M., Kirz, J., Howells, M. R., Chang, P., Coane, P. J., Feder, R., Houzego, P. J., Kern, D. P. & Sayre, D. (1984). *X-ray Microscopy,* edited by G. Schmahl & D. Rudolph, pp. 203–215. Berlin: Springer-Verlag.
Safranek, J. (1998). Personal communication.
Samson, J. A. R. (1967). *Techniques of Vacuum Ultraviolet Spectroscopy*. New York: Wiley.
Sayre, D. & Chapman, H. N. (1995). *Acta Cryst.* A**51**, 237–252.
Trebes, J. E., Brown, S. B., Campbell, E. M., Matthews, D. L., Nilson, D. G., Stone, G. F. & Whelan, D. A. (1987). *Science*, **238**, 517.
Vogt, S., Chapman, H. N., Jacobsen, C. & Medenvaldt, R. (2000). *Ultramicroscopy*. To be published.
Wang, Y., Jacobsen, C., Maser, J. & Osanna, A. (2000). *J. Microsc.* **197**, 80–93.